Journal of Materials Chemistry A

Accepted Manuscript

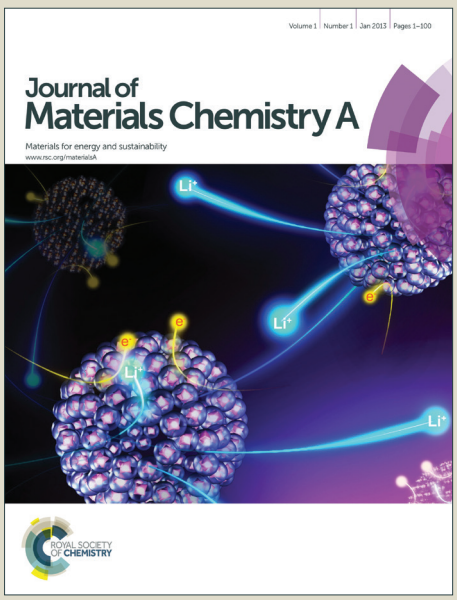

ROYAL SOCIETY OF CHEMISTRY

www.rsc.org/materialsA

Journal Name ARTICLE

Investigation of In-doped $BaFeO_{3-\delta}$ perovskite-type oxygen permeable membranes

Cite this: DOI: 10.1039/x0xx00000x

Yao Lu[a], Hailei Zhao*[,a,c], Xing Cheng[a], Yibin Jia[a], Xuefei Du[a], Mengya Fang[a], Zhihong Du[a], Kun Zheng[b], Konrad Świerczek[b]

Received 00th January 2012,
Accepted 00th January 2012

DOI: 10.1039/x0xx00000x

www.rsc.org/

Cobalt-free $BaFe_{1-x}In_xO_{3-\delta}$ perovskites, with Fe partially substituted by indium at B-site, were synthesized by a conventional solid state reaction and systematically characterized in terms of their phase composition, crystal structure, thermal reducibility, oxygen permeability, as well as structural stability in order to evaluate their application as oxygen permeation membranes. Introduction of more than 10 at.% of In in $BaFe_{1-x}In_xO_{3-\delta}$ causes a formation of single phase material with cubic perovskite structure, which exhibits no phase transition during cooling process. Thermal reducibility and thermal expansion coefficient are effectively reduced by indium doping, owing to the less changes of concentration of the oxygen vacancies in these compounds. However, In occupying B-site breaks B-O-B double exchange mechanism, and thus results in a gradual decrease of the electrical conductivity upon doping. Rietveld refinement and first principle calculation were performed to get an insight into the In influence on lattice structure, oxygen migration energy and electron conduction behaviour of $BaFe_{1-x}In_xO_{3-\delta}$. When using He/Air as sweep/feed gas, the $BaFe_{0.9}In_{0.1}O_{3-\delta}$ dense membrane with 1.0 mm thickness features a high oxygen permeation flux of 1.11 mL cm^{-2} min^{-1} at 950 °C. The observed good performance is attributed to the relatively high concentration of oxygen vacancies and low energy barrier for oxygen ion migration. It is also found that for membranes thinner than 0.8 mm, the oxygen flux is no longer limited by the bulk diffusion, while the oxygen surface exchange process becomes the dominant factor.

1 Introduction

Oxides with high and mixed ionic-electronic conductivity (MIEC) have been extensively studied because of their potential applications in oxygen separation technology,[1-3] Solid Oxide Fuel Cells (SOFCs),[4-6] and chemical process for conversion of hydrocarbons to syngas.[7-9] Among these applications, oxygen permeable membranes and membrane reactors for partial oxidation of methane (POM) utilising MIEC materials have attracted worldwide attention owing to their exceptional economic and environmental advantages. For the sake of practical application, these dense membranes should deliver high oxygen permeation flux and possess very good thermal stability as well as suitable mechanical properties under severe operating conditions.[10]

Oxygen transport through dense MIEC membranes is driven by the oxygen partial pressure gradient present on the opposite sides of the sinter. Oxygen ions migrate from oxygen-rich side to the oxygen-lean side, at the same time, in order to maintain charge balance in the material, electrons transport in the opposite direction. Various complex oxides possess good MIEC properties, and among them materials having perovskite, brownmillerite, fluorite or Ruddlesden-Popper-type structures are well known.[11-13] Physicochemical properties of these oxides are defined by chemical composition, and for instance, $ABO_{3-\delta}$ (A: selected lanthanides, Ba, Sr, Ca; B: selected 3*d* metals, Nb, Ce, *etc.*) perovskite-type oxides can exhibit excellent electronic and ionic conductivity.

Many efforts have been made in order to optimize various properties of oxygen permeation membranes. Teraoka *et al.* prepared series of $La_{1-x}Sr_xCo_{1-y}Fe_yO_{3-\delta}$ materials with different composition and found that $SrCo_{0.8}Fe_{0.2}O_{3-\delta}$ showed the highest oxygen permeation flux of 3.1 mL min^{-1} cm^{-2} (STP) at 850 °C, as recorded for 1 mm thick membrane. This was attributed to an increase of the oxygen vacancy concentration (δ) when La^{3+} cations were substituted with Sr^{2+} ones, as well as the weaker bond energy for Co-O than Fe-O.[14] Systematic researches about an effect of doping various cations in $LaCoO_3$ on the oxygen permeability were also reported.[15,16] It was found that the ionic conductivity could be greatly enhanced by an introduction of lower valence cations on A and/or B sites. The recorded oxygen permeation flux was found to decrease in the following sequence Ba > Ca > Sr > Na for A-site substituted $La_{0.6}A_{0.4}Co_{0.8}Fe_{0.2}O_{3-\delta}$, while for B-site doping in $La_{0.6}Sr_{0.4}Co_{0.8}B_{0.2}O_{3-\delta}$ materials, the descending order is: Cu > Ni > Co > Fe > Cr > Mn.

Due to the reported high oxygen permeability for cobalt-based perovskite materials, many researchers concentrated their efforts on these compounds. Unfortunately, the order-disorder transition of oxygen vacancy was apparently observed upon $SrCo_{0.8}Fe_{0.2}O_{3-\delta}$ materials under low oxygen partial pressure which would cause the degradation of oxygen permeation fluxes and mechanical failures.[17,18] To fix these problems, Shao *et al.* proposed introduction of barium at the A-site of $SrCo_{0.8}Fe_{0.2}O_{3-\delta}$, of which the substitution was found not only to enhance structural stability of the materials, but also cause an improvement of the observed oxygen permeability. These changes were attributed to the adjustment of tolerance factor *t* and high concentration of disordered oxygen vacancies.[19]

However, with the intensified studies on cobalt-based materials, some other problems came up. Co-containing compounds can be easily reduced and also decomposed under low oxygen partial pressures at elevated temperatures, with precipitation of metallic Co, metal oxides or other phases.[20-22] Large radius change of cobalt cations during reduction (chemical expansion effect[23]) and possible decomposition may cause failure of Co-containing oxygen permeation membrane, which can be particularly dangerous at high temperatures under large oxygen partial pressure gradients and during long-term operation. These, in turn, limit practical application of such materials. In order to improve structural stability, researchers tried to introduce fixed-valence Nb, Zr or Ta elements at the B-site of $BaCo_{1-x-y}Fe_xM_yO_{3-\delta}$.[24-26] Although the partially substituted compounds exhibited somewhat better properties, it seems that only complete removal of cobalt from the chemical composition of candidate MIEC membrane materials can bring significant progress and solve stability issues.

There are already many reports concerning novel, cobalt-free oxygen permeable materials, such as $Ba_{0.5}Sr_{0.5}Fe_{1-y}M_yO_{3-\delta}$ (M: Al, Zn, Cu),[27-29] $BaFe_{1-x}M_xO_{3-\delta}$ (M: Y, Ce, Zr, La, Cu, Ni, Nb),[30-35] as well as $La_{0.7}Sr_{0.3}Fe_{0.6}Ga_{0.4}O_{3-\delta}$.[36] Most of these Co-free MIEC oxides are developed on a basis of the parent $BaFeO_{3-\delta}$. Owing to a stronger reduction resistance of iron cations, $BaFeO_{3-\delta}$-based compounds having cubic, perovskite-type structure exhibit higher chemical stability and good mechanical integrity. Furthermore, they were also successfully applied as a promising cathode materials for SOFCs,[37, 38] which is due to a high oxygen vacancy concentration present in these compounds at elevated temperatures, favorable electrochemical activity, and a high mobility of oxygen ions. All the mentioned properties are also important for developing good oxygen permeation materials. Besides, comparing to cobalt, much lower price and wider availability of iron are also beneficial in terms of the considered industrial applications.

Accordingly, the $BaFeO_{3-\delta}$-based materials have been regarded as one of the best candidates for oxygen separation technology. However, one important issue has to be overcome, as the stable crystal structure of the parent material is not the perovskite-type but hexagonal one.[31] Considering ionic radii of A- and B-site cations in $BaFeO_{3-\delta}$ (1.61 Å for Ba^{2+} in 12-fold coordination, 0.645 Å / 0.585 Å for HS Fe^{3+} / Fe^{4+} in 6-fold coordination[39]), one may notice that tolerance factor *t*, defined by Goldschmidt (Eq. 1),[40] is higher than unity, even assuming relatively high concentration of the oxygen vacancies.

$$t = \frac{r_A + r_O}{\sqrt{2}\left(r_B + r_O\right)} \quad (1)$$

where r_A, r_B and r_O are the ionic radii of A- and B-site cations, as well as oxygen anions, respectively,

In such case, perovskite-type structure is not stable, because small B-site cations (Fe) cannot form sufficiently big BO_6 octahedra to adjust to the big A-site (Ba) cations, and alternatively, the mentioned hexagonal structure, which unfortunately does not show good MIEC properties, is being formed.[31,34]

In order to obtain good electronic and ionic transport, $BaFeO_{3-\delta}$-based materials should exhibit perovskite-type, and preferably, cubic structure, in which tolerance factor is equal or close to one. In such structure, oxygen vacancies are disordered and isotropous oxygen ion transmission routes are present. Apparently, it is possible to decrease *t* by means of an appropriate doping strategy, which can be done by replacing barium with smaller cations or iron with larger ones. Unfortunately, Li *et al.* reported that the lattice free volume and the oxygen vacancy concentration were reduced by partial substitution of barium with smaller strontium cations, which resulted in deterioration of the oxygen permeation performance of the membranes.[41] Thus, partial substitution of iron with cations having larger radius come to be a more reasonable way. In this case, not only the structural mismatch could be reduced, but also an open space would be expanded in the unit cells for oxygen ion migration. Moreover, the oxygen vacancy concentration may be also simultaneously increased, by selecting low valence cations as dopant. All these aspects would eventually promote the oxygen permeability of membranes.

Among candidate dopant cations, indium seems to be a perfect choice, due to its various special characteristics. In^{3+} ionic radius in 6-fold coordination is equal to 0.8 Å, and is sufficiently larger than the respective radii of Fe^{3+} and Fe^{4+}. Stable +3 charge state of indium is lower than that of iron, which should increase δ in the doped $BaFe_{1-x}In_xO_{3-\delta}$. Therefore, two beneficial effects can be expected for materials partially doped with indium in the B-site: stabilization of the cubic structure, resulting from a decrease of the tolerance factor, and an increase of concentration of the oxygen vacancies, due to a decrease of the average oxidation state of B-site cations. However, one more positive aspect should also be considered: comparing to Fe-O bond, the lower average bond energy of In-O can reduce constraints of the B-site cations in BO_6 octahedra, which should be favorable for transport of the oxygen anions *via* oxygen vacancy mechanism.

Combining all the presented above advantages, choice of In doping in $BaFe_{1-x}In_xO_{3-\delta}$ series seems to be the most suitable one. To the best of our knowledge, this paper presents for the first time systematic investigations of the crystal structure, electrical conductivity, oxygen permeability, and structural stability of $BaFe_{1-x}In_xO_{3-\delta}$materials. The observed relationship between structural properties, electrical conductivity and the electro-chemical performance of these compounds is also discussed.

2 Experimental

2.1 Synthesis of the materials and preparation of membranes

$BaFe_{1-x}In_xO_{3-\delta}$ (x = 0.05-0.2) oxides were prepared by a conventional solid state reaction method. $BaCO_3$, Fe_2O_3 and In_2O_3 raw materials (all A.R. purity) were weighed in a stoichiometric ratio and then ball-milled in ethyl alcohol for 4 h

at 400 rpm. After drying in oven for 12 h, the powders were calcined at 1000 °C in air for 10 h. The obtained powders were thoroughly ground in a mortar, to break the agglomerates, which was followed by an additional ball-milling performed for 4 h. The dried powders were pressed into disks (Φ ~19 mm, thickness of 1-2 mm) and bars (4 mm × 7.5 mm × 42 mm) under uniaxial pressure of 110 MPa, with 1 wt.% of PVA being added. The green samples were then sintered at 1300-1320 °C for 7 h in air, with heating and cooling rates of 3 °C min^{-1}, which allowed to achieve similar relative density of the sinters. Sintered disks were polished to a proper thickness for the oxygen permeation examinations. Bulk density of the sintered bars was measured by Archimedes' method, using distilled water as medium. The relative density values were derived from the measured bulk density and from the theoretical density, which was calculated on the basis of the refined lattice parameters. The sintering temperature and the calculated relative density for each compound are shown in Table 1.

2.2 Structural characterization

Phase composition and crystal structure of the as-sintered samples and these after oxygen permeation tests were examined by X-ray diffraction (XRD) method using Rigaku D/max-A diffractometer. Measurements were conducted with Cu $K_{\alpha 1}$ radiation (λ = 1.5406 Å) in 10-100° range. Additional high temperature studies in air up to 900 °C were performed on Panalytical Empyrean diffractometer equipped with Anton Paar 1200N oven-chamber and PIXcel3D detector. For these measurements, the sintered dense samples were ground into powders. Temperature program was set up with 10 °C min^{-1} heating and cooling rates, while data were gathered with 100 °C step in 10-110° range. Before each scan, which was lasting for about 50 min, sample was equilibrated at the particular temperature for 5 min. Rietveld method was applied to refine the recorded XRD patterns using General Structure Analysis System (GSAS) with the EXPGUI graphical user interface.[42,43]

In order to investigate structural stability under reducing atmosphere, the samples were annealed at 800 °C for 10 h in flowing 5 vol.% H_2 in Ar gas mixture, after which XRD method was used to test structural changes of the surface of $BaFe_{1-x}In_xO_{3-\delta}$ membranes.

2.3 Thermal properties analysis and electrical conductivity measurements

Oxygen temperature-programmed desorption process (O_2-TPD) was carried out to investigate oxygen desorption properties using Quantachrome Instruments ChemBET Pulsar TPD/TPR analyzer. Approximately 200 mg of powder was loaded in a quartz tube, which was placed in a tubular furnace controlled by a thermocouple. Temperature of the furnace was then raised from room temperature to 900 °C with 10 °C min^{-1} rate, while an online TCD detector tested the released oxygen, using pure argon as a carrier gas at flow rate of 50 mL min^{-1}.

Weight changes of $BaFe_{1-x}In_xO_{3-\delta}$ samples as a function of temperature were characterized by thermogravimetric analysis (TG) on Netzsch STA 449 apparatus in air between room temperature and 1000 °C. For the studies, air flow rate of 60 mL min^{-1} was used. Based on these results, and on the values of the initial oxygen nonstoichiometry δ_0, which were evaluated from iodometric titration method,[37,38] the oxygen nonstoichiometry at the high temperatures δ_t was calculated using the Eq. 2.

$$\delta_t = \delta_0 + \frac{(m_0 - m_t)\times(M - 15.9994\delta_0)}{15.9994 m_0} \quad (2)$$

where m_0 is the initial and m_t the actual weight of the sample at the particular temperature, and M is the molar mass of $BaFe_{1-x}In_xO_3$ with stoichiometric oxygen content.

For thermal expansion coefficient (TEC) measurements, the sintered bars were polished to a proper size. Studies were conducted in air using Netzsch DIL 402/PC dilatometer from room temperature to 1000 °C with a heating rate of 5 °C min^{-1}. Electrical conductivity of the samples was measured by a four-probe DC method in air atmosphere at temperatures ranging from 200 to 900 °C. The sampling interval for data acquisition was 50 °C, while at each temperature the sample was hold for 15 minutes, after which the recorded values were constant.

2.4 Oxygen permeation measurements

The oxygen permeation properties of the considered $BaFe_{1-x}In_xO_{3-\delta}$ membranes were measured by gas chromatography method using a vertical high temperature oxygen permeation apparatus described in previous work.[33] After being polished, the as-prepared $BaFe_{1-x}In_xO_{3-\delta}$ membranes, with a thickness of 0.6-1.2 mm, were sealed on one alumina tube, with an effective inner circular area of 1.09 cm^2, by commercially available binder (Aremco Products. Inc., Ceramabond 552-VFG). Compressed air was supplied to the alumina tube as the feed gas, with a flow rate of 120 mL min^{-1} [STP]. On the other side of the membrane, a high purity helium (> 99.999%), was introduced into another alumina tube as a carrier gas, with flow rate of 60 mL min^{-1} [STP]. The outlet gas, being a mixture of helium and permeated oxygen, was then introduced into the gas chromatograph with TCD (GC, SP2100). In the present work no nitrogen leaks were detected, confirming that the membranes were well sealed and were gas-tight. The oxygen permeation flux was calculated using Eq. 3.

$$J_{O_2}(\mathrm{mL\,cm^{-2}\,min^{-1}}) = \frac{C_{O_2}}{1 - C_{O_2}} \times \frac{F}{S} \quad (3)$$

where C_{O2} stands for the measured oxygen concentration in the outlet gas on the sweep side, F is the flow rate of the helium,

Table 1 Sintering temperature and relative density of $BaFe_{1-x}In_xO_{3-\delta}$ (x = 0.05-0.2) samples.

Composition	Sintering temperature [°C]	Relative density [%]
$BaFe_{0.95}In_{0.05}O_{3-\delta}$	1300	95.2
$BaFe_{0.9}In_{0.1}O_{3-\delta}$	1320	93.4
$BaFe_{0.85}In_{0.15}O_{3-\delta}$	1320	94.9
$BaFe_{0.8}In_{0.2}O_{3-\delta}$	1320	91.8

and S is the effective inner circular area of membrane for oxygen permeation.

Gas flow rates were monitored by a mass flow meter (Sevenstar, DC-07). The oxygen permeation properties of 1 mm thick $BaFe_{1-x}In_xO_{3-\delta}$ membranes with different compositions were examined in the temperature range from 800 to 950 °C. To elucidate the kinetic process of oxygen permeation involving surface oxygen exchange and bulk oxygen migration, changes of the oxygen permeability were recorded for selected $BaFe_{0.9}In_{0.1}O_{3-\delta}$ membrane with various thicknesses.

2.5 First principles calculations

In order to explore the effect of indium doping on transport of the oxygen anions, the oxygen migration barrier energies were calculated through CASTEP (Cambridge Serial Total Energy Package) code,[44, 45] which is based on the density-functional theory (DFT) and plane-wave pseudopotential (PWP) method. For the exchange-correlation potential in the generalized gradient approximation (GGA), the Perdew-Burke-Ernzerhof (PBE) scheme was employed.[46] The cutoff energy of the plane waves was chosen at 300 eV, and the atomic coordinates of the simulated structures were optimized by an iterative process using Broyden-Fletcher-Goldfarb-Shanno (BFGS) algorithm,[47] in order to minimize the energy with respect to the atomic positions. Tolerance for a self-consistence was set at: 2×10^{-5} eV atom^{-1} for total energy, 0.05 eV Å^{-1} for force, 0.1 GPa for maximum stress, and 0.002 Å for the maximum displacement. The Brillouin zone integrations were approximated using special 2×2×2 k-point sampling scheme of Monkhorst-Pack for the unit cell.[48] The valence electronic configurations were taken as: O-$2s^2 2p^4$, Fe-$3d^6 4s^2$, In-$4d^{10} 5s^2 5p^1$ and Ba-$5s^2 5p^6 6s^2$, for the ground-state electronic structure calculations. Spin polarization calculation was adopted, and the formal spin was used as the initial one.

3 Results and discussion

3.1 Crystal structure

The calculated tolerance factors t depending on composition of $BaFe_{1-x}In_xO_{3-\delta}$ compounds using Eq. 1 are presented in Fig. 1. Three different lines are shown, corresponding to three different assumptions: as in $BaFe_{1-x}In_xO_{3-\delta}$, Fe cations can have mixed +3/+4 valence state, and Fe^{3+} cations in octahedral coordination can be in a high spin (HS) or a low spin (LS) configuration with different ionic radius. For the performed calculations, the average B-site radius was computed by weighting the ionic radius to take the proportion of cations into account. Every assumption gets closer to ideal conditions with increasing In content, suggesting a strong tendency for forming cubic perovskite structure. The room-temperature XRD patterns of $BaFe_{1-x}In_xO_{3-\delta}$ materials are shown in Fig. 2. The samples with x= 0.05 correspond to a rhombohedral structure, while a cubic perovskite structure is recognized for these with more than 10 at.% In substituting for Fe ions, indicating that In-doping can stabilize the cubic structure of $BaFeO_{3-\delta}$ down to room temperature, which is consistent with the calculated results of tolerance factors, as shown in Fig. 1. With increasing

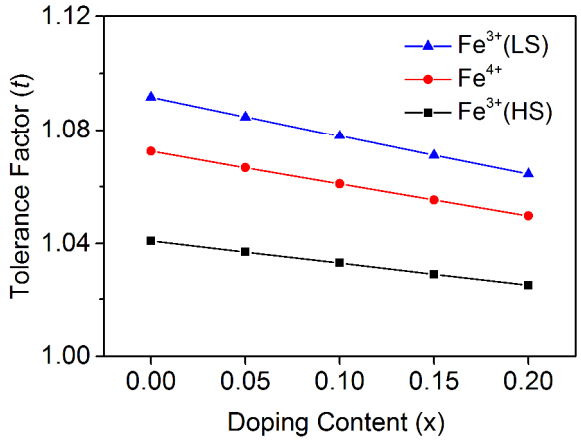

Fig. 1 Tolerance factor of $BaFe_{1-x}In_xO_{3-\delta}$ compounds calculated for three different assumptions about valence state of Fe cations.

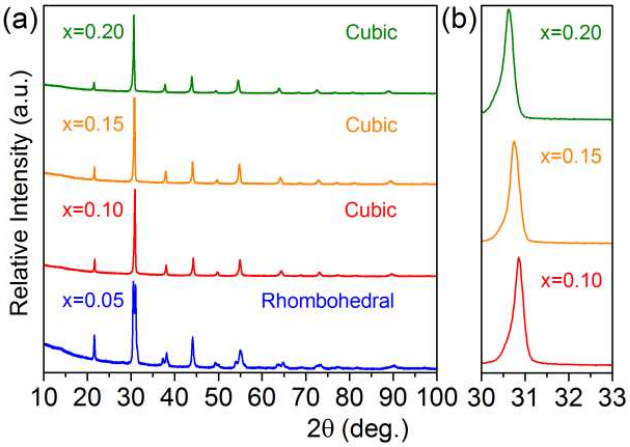

Fig. 2 XRD patterns recorded for $BaFe_{1-x}In_xO_{3-\delta}$ at room temperature in: (a) 10-100° range, (b) selected 30-33° range.

In-doping level, the peaks shift to lower degree gradually for x=0.1-0.2, as shown in the enlarged view of Fig. 2b, which is associated with the larger ionic size of In^{3+} than that of $Fe^{3+/4+}$ and is an indicative of In ions having dissolved in $BaFeO_{3-\delta}$ lattice.

3.2 Structural evolution at high temperatures

Fig. 3 shows results of high temperature structural studies of the considered $BaFe_{1-x}In_xO_{3-\delta}$ materials. Samples with x = 0.1-0.2 are found to exhibit cubic structure with no detectable impurities in whole studied temperature range from 25 °C to 900 °C, while compound with x = 0.05 displays a complex phase structure. Initially, in the vicinity of 400 °C, a reversible phase transition between rhombohedral and cubic structure occurs. The observed major structural transition process seems to be related to the electron state transition of Fe^{3+} from the low spin to high spin.[37,38,49] Also, thermal reduction of Fe cations

would reduce a mismatch between A- and B-site cations and, as a result, the phase transition to cubic perovskite structure occurs for $BaFe_{0.95}In_{0.05}O_{3-\delta}$. However, there some secondary phases appear when temperature rises to 900 °C as shown in the inset of Fig. 3a and still can be found even after cooling to room temperature. To obtain more structure information, the XRD patterns of samples with x=0.05 at 25 °C and 900 °C were subjected to crystal structure refinement through Rietveld method. As shown in Fig. 4, the refinement results indicate that before heating the structure of $BaFe_{0.95}In_{0.05}O_{3-\delta}$ has a good fit to a rhombohedral phase, while transforms to a mixture of an orthorhombic phase $BaFe_{2-y}In_yO_4$ and cubic phase $BaFe_{1-x}In_xO_3$ at high temperature. Details about the refined structural parameters at considered temperature are listed in Table 2. The presence of 2.9 wt.% oxygen-ion insulating orthorhombic phase would eventually have an unfavourable effect of blocking the oxygen-ion conduction.[50]

The refined unit cell parameters as a function of temperature, for the studied $BaFe_{1-x}In_xO_{3-\delta}$ materials (x=0.01-0.2), are gathered in Fig. 5. Solid and dash lines represent heating and cooling processes, respectively. As can be observed, for all compounds the dependence is not linear in the measured range, and with an increase of the temperature up to 200 °C, the lattice parameter *a* initially increases, but then decreases, and further

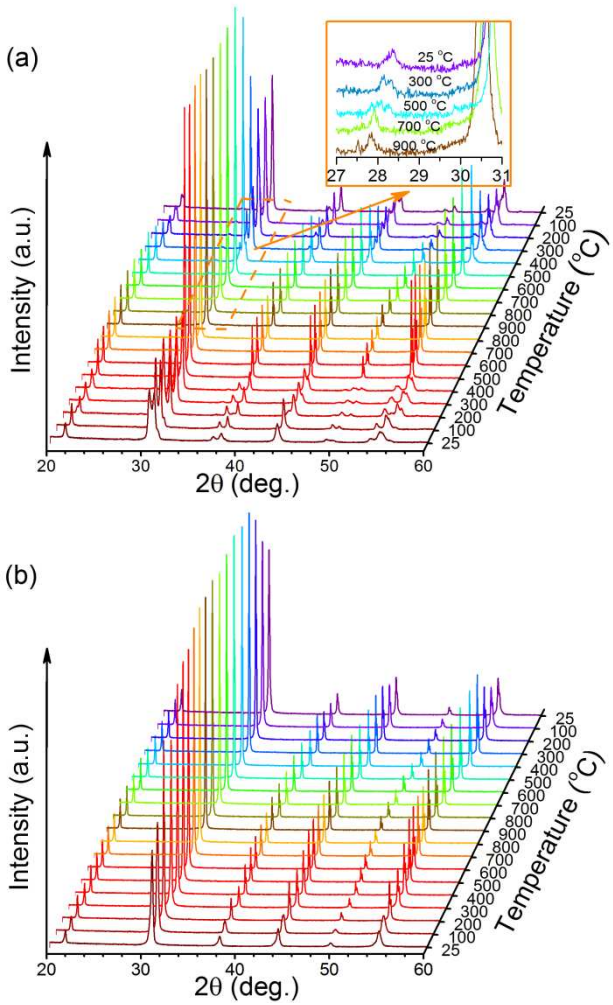

Fig. 3 HT-XRD patterns of $BaFe_{1-x}In_xO_{3-\delta}$ powders for: (a) x = 0.05, (b) x = 0.1.

increases above 400 °C. During cooling, *a* parameter decreases steadily, but with a change of slope below 500 °C. The dependence on heating overlap with the one recorded on cooling very well in the high temperature range (≥500 °C) for all samples. However, a rather big difference in values and shape of the curves can be seen at lower temperatures. This result may be explained by taking into account a fact that the powder samples used for HT-XRD examination were obtained from the crushed dense pellets, so it is expected that the oxygen vacancy concentration before and after the heating/cooling cycle were changed in the materials. During the sintering process, more oxygen vacancies are generated at high temperatures, while on cooling, the oxygen is incorporated back

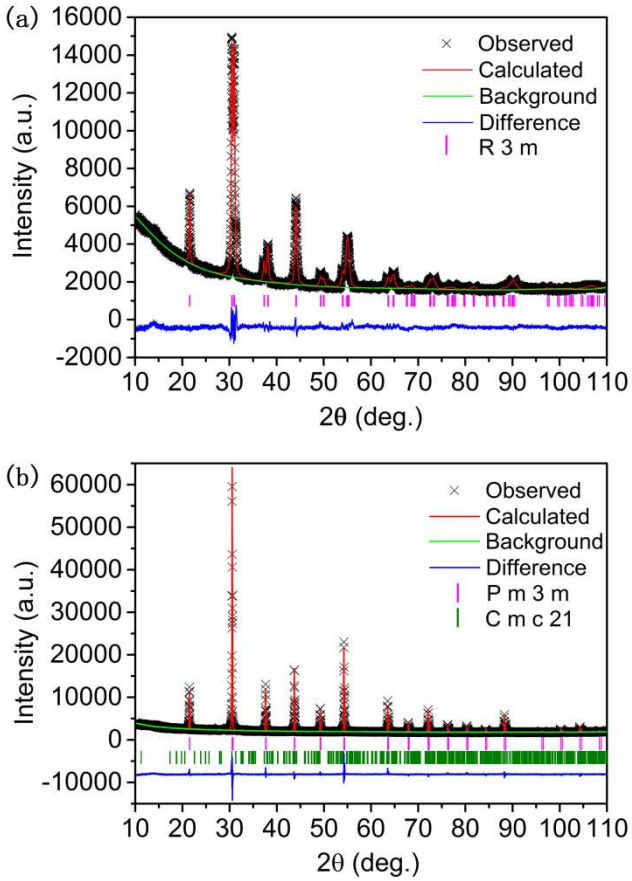

Fig. 4 Rietveld refinement of XRD patterns for $BaFe_{0.95}In_{0.05}O_{3-\delta}$ powders at different temperatures: (a) 25 °C before heating, (b) 900 °C.

Table 2 Refined structural parameters of $BaFe_{0.95}In_{0.05}O_{3-\delta}$ compounds at different temperatures.

	25 °C (before heating)	900 °C	
Space group	R3m	Cmc21	Pm-3m
Unit cell parameter a [Å]	4.0982(3)	8.68(1)	4.1413(1)
Unit cell parameter b [Å]		19.01(2)	
Unit cell parameter c [Å]		5.46(1)	
α = β = λ [deg]	89.12(1)	90	90
Weight fraction [wt.%]	100	2.1(1)	97.9(1)
Rwp [%]	3.77	4.37	
Rp [%]	2.79	2.90	
χ2	3.312	4.344	

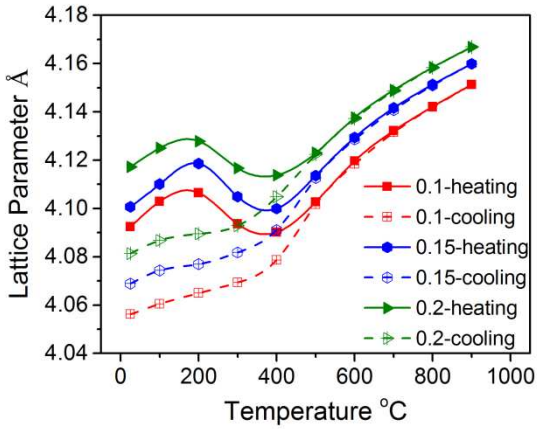

Fig. 5 Temperature dependence of the lattice parameters of $BaFe_{1-x}In_xO_{3-\delta}$ (x = 0.1, 0.15 and 0.2), calculated from refinement of the HT-XRD results.

into the material. This process is easy to reach the thermodynamic equilibrium at high temperatures (≥500 °C) but difficult at low temperatures. It is known that the oxygen uptake is a kinetically controlled process. Initially, the oxygen is incorporated into the active sites at the surface, generating oxygen concentration gradient between the surface and the bulk. Then, the oxygen anions from the surface migrate into the material, while the oxygen vacancies diffuse toward surface. For dense sinters, diffusion length is comparable to the dimensions of the sample, and the diffusion time can be relatively long, especially at lower temperatures. This is often observed if the activation energy of the chemical oxygen diffusion is large, as well as for thick samples. It is therefore expected that the oxygen vacancy concentration in the sintered pellets was higher than the equilibrium one, especially at lower temperatures.

For the conducted HT-XRD measurements, the dense pellets were crushed into fine powders. In the heating process, the lattice parameters first increased with the temperature, due to the thermal expansion effect. When the temperature reached a point, at which diffusion became fast enough, the materials would absorb oxygen from atmosphere, which had enough time to diffuse through the crystal lattice, leading to a decrease of the lattice parameters. After the equilibrium was reached, the lattice parameters displayed an increasing tendency, owing to the thermal and chemical expansion. In the cooling process, the observed changes of the unit cell parameters are closer to the equilibrium one at lower temperatures. Likely, below 300 °C no changes of the oxygen content occur, and the oxygen content in the materials after cooling is close to the equilibrium one. The presented above behaviour was fully supported by the thermo-gravimetric studies presented in chapter 3.4 below.

3.3 Thermal properties

HT-XRD data on cooling were used for calculation of linear TECs. The calculated TEC values for three different $BaFe_{1-x}In_xO_{3-\delta}$ samples are listed in Table 3. At the same time, dilatometry studies were conducted on dense bars of two

samples with x = 0.1 and 0.2 to get the tested TEC values (Fig. S1). As presented in Table 3, no matter what measurement method is employed, the TEC values in high temperature range are much higher than that in low range, which is mainly attributed to the chemical expansion effect originating from changes of the oxygen content. It is obvious that In-doping allowed to decrease the TEC of the investigated materials regardless of the temperature range.

Comparing HT-XRD and dilatometry studies, an evident discrepancy can be seen in the lower temperature range, however, it can be easily explained, considering a different procedure of the experiments. Analysing data presented in Fig. 5, it can be observed that during initial heating, up to about 200 °C, unit cell parameters of all the materials increase more strongly on temperature than on cooling in the same temperature range. As the dilatometry measurements were conducted on heating, it is not unexpected that the reported TECs are much higher than the ones calculated from HT-XRD on cooling, which is owing to the presence of high oxygen vacancy concentrations in the dilatometry samples.[51,52] Because the samples were in a form of dense sinters, oxygen incorporation, occurring for the powdered materials above 200 °C, was not fast enough to influence thermal expansion up to about 400 °C. Above 700 °C both experiments give similar thermal expansion, which indicates that changes of the oxygen content in the bars are fast enough to follow oxygen stoichiometry changes in the powders. Somewhat smaller TECs from dilatometry studies may be related to a presence of pores, which buffer, to some degree, the thermal expansion.

The O_2-TPD results (Fig. S2) provide evidence for lattice oxygen release at high temperature, which is often associated with thermal reduction of variable valence cations and formation of oxygen vacancies. They will cause increased ionic radius and enhanced repulsion of the electron cloud around vacancy to induce the mentioned chemical expansion of the oxide lattice.[53-55] Comparing to $BaFe_{0.9}In_{0.1}O_{3-\delta}$, the slightly reduced area of the oxygen desorption peak for $BaFe_{0.8}In_{0.2}O_{3-\delta}$ suggests that the oxygen anions become more stable in the crystal lattice for materials with higher indium content. Different onset temperatures for the oxygen release (comparing Figs. 5, S1 and S2), recorded by different experimental techniques, may be directly associated with varying experimental conditions, especially regarding sample's form (powder, pellet), heating/cooling rates and the atmosphere, in which the studies were conducted.

It should be mentioned that TEC of $BaFe_{0.9}In_{0.1}O_{3-\delta}$ at higher temperatures, equal to 22.4×10^{-6} K^{-1}, has been improved, comparing to many considered Co-based materials for oxygen permeation membranes, which is beneficial from a point of view of application.[56-58]

3.4 Oxygen nonstoichiometry

For evaluation of In-doping effect on the oxygen vacancy concentration, thermogravimetric analysis was conducted for $BaFe_{1-x}In_xO_{3-\delta}$ materials (x = 0.1-0.2). The results of these studies are shown in Fig. S3a. On the initial heating, all materials show weight loss, occurring from room temperature to about 250 °C, which can be attributed to a desorption of physically absorbed water and gases.[59,60] Above this temperature weigh remains almost constant, but near 330 °C it starts to increase, but ends at 420-440 °C. This behaviour corresponds well to the structural studies (Fig. 5), and can be explained by the incorporation of oxygen. At higher temperatures significant weight loss is noticed for all of the samples, while on cooling, it increases continuously down to 300 °C. Assuming that on the initial heating, below 300 °C, all the observed changes are due to desorption-related processes, the oxygen nonstoichiometry values evaluated from the iodometric titration (δ_0) and TG results can be used for calculating the temperature dependence of oxygen nonstoichiometry (δ_t). The computed values are displayed in Fig. S3b, while Table 4 shows data at selected temperatures.

As shown in Fig. S3b, δ can exceed 0.5, especially at high temperatures, indicating complex defect structure in the materials. Indeed, this requires presence of some iron cations having +2 oxidation state. Taking this into account, the recorded TG data can be explained in the following way: initially, in order to restore the equilibrium state, on heating in the 350-450 °C temperature range, the oxygen is incorporated, and this process corresponds to a shift of the presented below reaction (Eq. 4) towards oxidation of Fe^{3+} (to the left):[19]

$$2Fe_{Fe}^{\bullet} + O_O^X \leftrightarrow 2Fe_{Fe}^X + V_O^{\bullet\bullet} + \frac{1}{2}O_2 \uparrow \qquad (4)$$

However, at higher temperatures, the equilibrium is shifted to the right, with getting the partial reduction of Fe^{4+} back to dominant position. Furthermore, at even higher temperatures, δ exceeds 0.5, and presence of Fe^{2+} cations can be expected as shown in Eq. 5.

$$2Fe_{Fe}^X + O_O^X \leftrightarrow 2Fe_{Fe}^{'} + V_O^{\bullet\bullet} + \frac{1}{2}O_2 \uparrow \qquad (5)$$

After heating and cooling processes, the equilibrated oxygen

Table 3 Thermal expansion behaviour of the considered $BaFe_{1-x}In_xO_{3-\delta}$ perovskites. TEC units [10^{-6} K^{-1}].

Composition	TEC from HT-XRD on cooling		TEC from dilatometry	
	25-300 °C	600-900 °C	25-500 °C	700-1000 °C
$BaFe_{0.9}In_{0.1}O_{3-\delta}$	11.3	26.5	19.3	22.4
$BaFe_{0.85}In_{0.15}O_{3-\delta}$	10.9	24.3		
$BaFe_{0.8}In_{0.2}O_{3-\delta}$	9.7	23.8	18.5	20.9

Table 4 Oxygen nonstoichiometry of $BaFe_{1-x}In_xO_{3-\delta}$ (x = 0.1, 0.15 and 0.2) samples at selected temperatures.

Composition	δ			
	RT as-synthesized	800 °C	900 °C	RT after TG experiment
$BaFe_{0.9}In_{0.1}O_{3-\delta}$	0.51	0.59	0.60	0.38
$BaFe_{0.85}In_{0.15}O_{3-\delta}$	0.48	0.55	0.55	0.36
$BaFe_{0.8}In_{0.2}O_{3-\delta}$	0.46	0.51	0.52	0.39

nonstoichiometry in the samples is much smaller than the initial one.

Analysing data presented in Table 4, a strong negative correlation can be noticed between In content and the oxygen nonstoichiometry, with values of δ decreasing with the doping level. This shows that indium impedes oxygen loss from the lattice, likely ensuring better structural stability of the compounds.

3.5 Electrical conductivity

The measured total electrical conductivity of $BaFe_{1-x}In_xO_{3-\delta}$ (x = 0.05-0.2) samples, conducted in 200-900 °C temperature range in air, are plotted in Fig. 6. As for majority of similar perovskite-type MIECs, the electronic conductivity is at least one or more orders of magnitude higher than the oxygen ionic conductivity,[61] the ionic contribution to the total conductivity can be neglected. As can be seen, for all samples, the electrical conductivity gradually increases with temperature up to about 550 °C, and then it saturates, with the maximum value decreasing from about 9.4 S cm^{-1} for $BaFe_{0.95}In_{0.05}O_{3-\delta}$ down to 2.3 S cm^{-1} for $BaFe_{0.8}In_{0.2}O_{3-\delta}$. A linear relationship in the Arrhenius-type plot, as shown in Fig. 6b up to about 550 °C, implies that the electronic conduction in $BaFe_{1-x}In_xO_{3-\delta}$ materials follows a small polaron conducting mechanism, with activation energy in 0.32-0.38 eV range. In this charge transfer mechanism small polaron hops are realized between multivalent metal (Fe) cations present at the B-site in so called Zerner double-exchange along B-O-B bonds, with oxygen anions actively participating.[62]

After reaching the maximum values at about 600 °C, the electrical conductivity decreases abruptly for all the materials. It can be considered as originating from release of the lattice oxygen at high temperatures, as documented for instance in Fig. S2. Because oxygen loss causes an increase of the oxygen vacancy concentration, the B-O-B charge transfer mechanism is affected, and at the same time, charger carrier concentration would be reduced. It can be noticed that generally, the electrical conductivity decreases with increasing indium doping level which can be mostly attributed to the decreasing concentration of iron cations, replaced with fixed-valence In^{3+} ions (In-O-Fe and In-O-In small polaron transport is not possible).

3.6 Oxygen permeation properties

The temperature dependence of the recorded oxygen permeation fluxes for $BaFe_{1-x}In_xO_{3-\delta}$ (x = 0.1-0.2) membranes with 1 mm thickness are shown in Fig. 7. Before analyzing data, it has to be emphasized that in the measured 800-950 °C temperature range, the kinetics of formation of the oxygen vacanies are fast enough for the membranes to be at equilibrium state.

With temperature rises, the oxygen permeation fluxes of all samples increase significantly. Considering the cubic phase being the major component in x=0.05 sample at around 400 °C (Fig. 4a), the oxygen permeation fluxes for all materials grow linearly in Arrhenius-type coordinates in the 800-950 °C range, without abrupt changes, which are unlikely for the pure $BaFeO_{3-\delta}$ oxide.[32] Nevertheless, the oxygen migration energy for x=0.05 is much larger than that of the samples with x=0.1-0.15, which is most probably due to the existence of some secondary orthorhombic phases that may block the oxygen-ion conduction. Taking the other samples (x=0.1-0.2) with single cubic perovskite structure into comparison, it is obvious that the oxygen permeability decreases with In content, while the

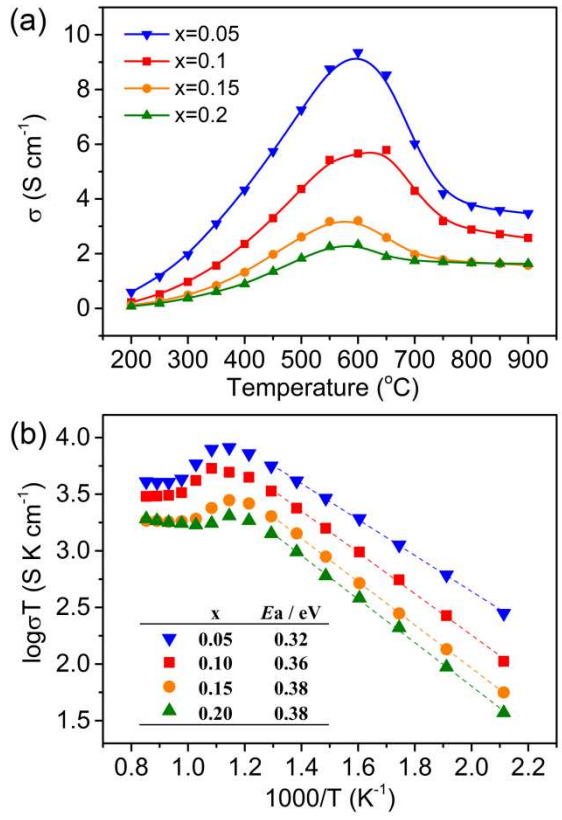

Fig. 6 (a) Temperature dependence of the electrical conductivity of $BaFe_{1-x}In_xO_{3-\delta}$ samples in air, and (b), in the corresponding Arrhenius-type plot.

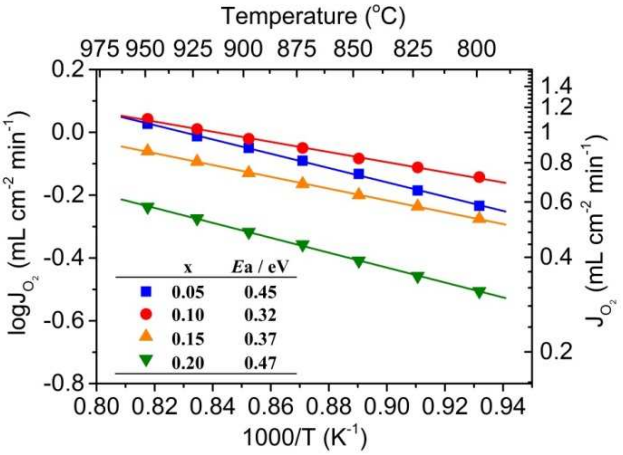

Fig. 7 Temperature dependence of the oxygen permeation fluxes through 1.0 mm thick $BaFe_{1-x}In_xO_{3-\delta}$ membranes (x = 0.05-0.2). Feed side: 120 mL min^{-1} air, permeate side: 80 mL min^{-1} He.

oxygen migration energy increases. The oxygen permeability for x=0.1 reaches the highest value of 1.11 mL cm^{-2} min^{-1} for 1 mm thickness at 950 °C. Since the oxygen vacancy concentration decreases with the increasing In content for x=0.1-0.2, as summarized in Table 4, the observed decrease of the oxygen permeation fluxes for the higher In content materials is not unexpected.

While, the increased Ea for oxygen ion migration with In-doping level drives people to seriously consider the change in lattice characters. It is known that the oxygen migration in perovskites is controlled by many factors, including the lattice free volumes (V_f), the critical radius (r_C), and the average bonding energy of metal-oxide (ABE).[63,64] Among them, the V_f plays an important role. This value is defined as the remaining volume of perovskite unit cell, after volume occupied by all ions is subtracted, and can be calculated using Eq. 6.

$$V_f = a^3 - \frac{4}{3}\pi\left[r_A^3 + r_B^3 + (3-\delta)r_O^3\right] \quad (6)$$

The calculated results of lattice free volume at 900 °C are presented in the Fig. 8 together with oxygen ion migration energy corresponding to In content. An expected dependence can be observed for materials with x = 0.1-0.2: the less the lattice free volume is, the higher the oxygen migration energy will be. So, the lattice free volume maybe has a great effect on oxygen ion migration energy and would be detrimental for oxygen permeability.

To further explore the oxygen transport mechanism through the considered membranes, the oxygen permeability studies of the most promising $BaFe_{0.9}In_{0.1}O_{3-\delta}$ material were conducted as a function of membrane thickness as shown in Fig. 9. It is known that the oxygen permeation through dense mixed-conducting oxide membrane not only depends on the bulk ionic diffusion, but also, depends on the electronic component of the conductivity, as expressed in the theoretical Eq. 7.[65]

$$J_{O_2} = -\frac{RT}{16F^2L}\int_{\ln P'_{O_2}}^{\ln P''_{O_2}} \frac{\sigma_{ion}\sigma_e}{\sigma_{ion}+\sigma_e} d[\ln P_{O_2}] \quad (7)$$

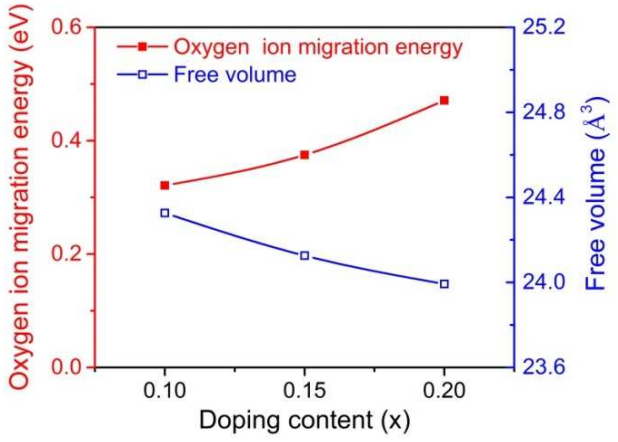

Fig. 8 Lattice free volume (V_F) in $BaFe_{1-x}In_xO_{3-\delta}$ (x=0.1-0.2) at 900 °C.as a function of In doping content (x) together with Oxygen ion migration energy (Ea)

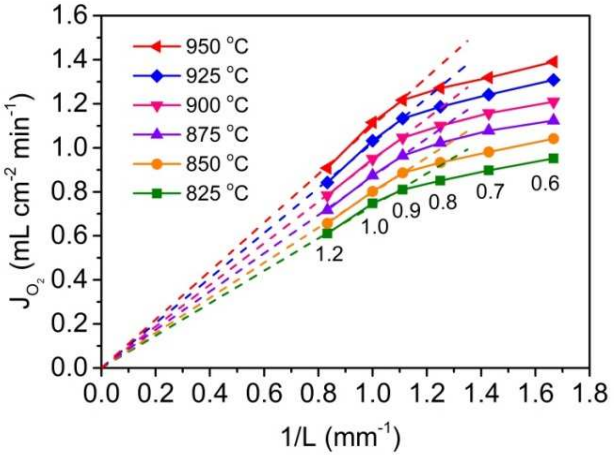

Fig. 9 Oxygen permeation flux dependence on the reciprocal thickness of the membrane, as measured at different temperatures for $BaFe_{0.9}In_{0.1}O_{3-\delta}$ samples.

where R, F, T, L, σ_e, and σ_i denote the gas constant, Faraday constant, temperature, thickness of the membrane, and electronic and ionic conductivities, respectively. In the Eq. 7, P'_{O2} stands for the oxygen partial pressure on the air side, while P''_{O2} means the oxygen partial pressure on the sweep side. Therefore, if the limiting step of the oxygen permeation is the bulk diffusion under constant oxygen partial pressure gradient, the relationship between oxygen permeation flux (J_{O2}) and the reciprocal of the membrane thickness ($1/L$) should be a straight line crossing the origin of coordinates. The oxygen permeation fluxes increase proportionally with $1/L$ when the thickness is larger than 0.8 mm at the whole temperature range from 825 °C to 950 °C as shown in the fitting dash line, however, when the thickness is decreased to below 0.8 mm, the oxygen permeation fluxes deviate from former tendency. The result clearly reveals that the total oxygen permeation process is mainly limited by the bulk diffusion of oxygen ions when the membrane thickness is greater than 0.8 mm, otherwise the limitation of the surface oxygen exchange reaction comes into playing an important role.

3.7 First principle calculation

The presented above results indicated importance of the In content on the oxygen ion diffusion in $BaFe_{1-x}In_xO_{3-\delta}$ oxides. Apart for experimental examinations, first principles calculations are of interest in such case, and these studies were also performed. For the computations, periodic supercells were constructed by expanding of the cubic unit cell of the perovskite up to 2×2×2 size, with certain number of iron atoms substituted by indium, corresponding to $BaFe_{0.875}In_{0.125}O_3$ ($Ba_8Fe_7InO_{24}$) and $BaFe_{0.75}In_{0.25}O_3$ ($Ba_8Fe_6In_2O_{24}$) compositions, as shown in Fig. 10. In the case of $Ba_8Fe_6In_2O_{24}$, two indium atoms are located at both ends of the diagonal, to keep them distant from each other for the sake of minimizing the system energy as expected in reality. After successfully completing geometry optimization, the optimized lattice parameters: 4.088 Å for $BaFe_{0.875}In_{0.125}O_3$ and 4.096 Å for $BaFe_{0.75}In_{0.25}O_3$ agree well with the experimental values of

4.056 Å and 4.081 Å, respectively, and these values were taken as constants during the following calculations of the energy barrier of the oxygen vacancy migration.

The oxygen vacancy migration barrier energies along different paths in the doped structures were evaluated basing on the models presented in our previous work.[61] One oxygen ion, which is adjacent to the oxygen vacancy is moved to the saddle point, at which the energy reaches the highest value during the oxygen ion migration process (Fig. 11).[66,67] The additional energy at this point is regarded as the energy barrier of the oxygen migration. As inducing another kind of cation into the B-sites, the coordination environment of oxygen ions and vacancies are changed and the structure considerations show

Table 5 Calculated energy barrier of the oxygen vacancy migration for different transport paths present in $BaFe_{0.875}In_{0.125}O_3$ and $BaFe_{0.75}In_{0.25}O_3$.

Migration barrier [eV]	$BaFe_{0.875}In_{0.125}O_3$		$BaFe_{0.75}In_{0.25}O_3$	
	[In-V_O-Fe]	[Fe-V_O-Fe]	[In-V_O-Fe]	[Fe-V_O-Fe]
[In-O-Fe]	4.43	1.98	4.33	2.72
[Fe-O-Fe]	1.50	1.29	2.14	2.07

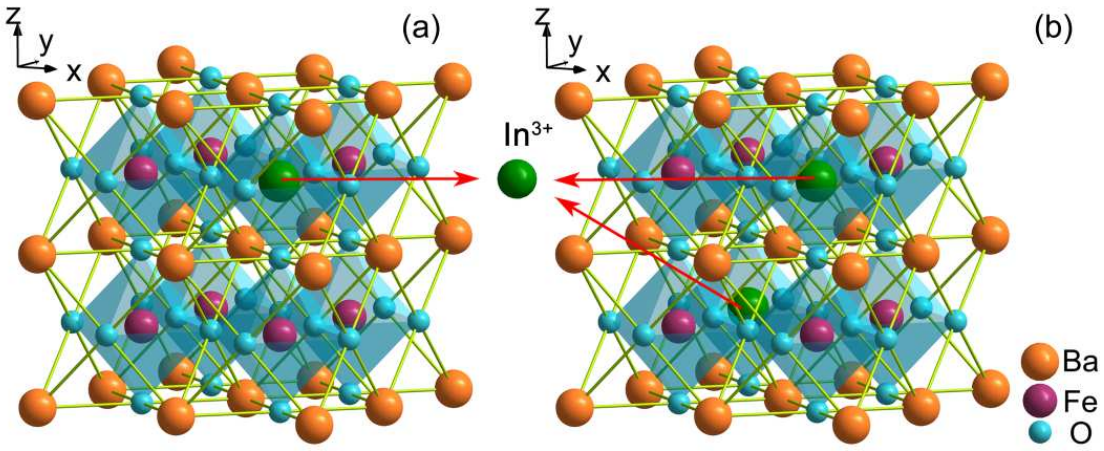

Fig. 10 Periodic supercells used for modeling: (a) $BaFe_{0.875}In_{0.125}O_3$ ($Ba_8Fe_7InO_{24}$), (b) $BaFe_{0.75}In_{0.25}O_3$ ($Ba_8Fe_6In_2O_{24}$).

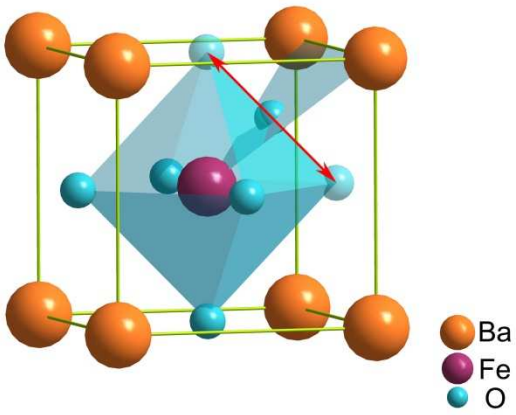

Fig. 11 Oxygen ion migration path from [FeOFe] to [FeV_OFe].

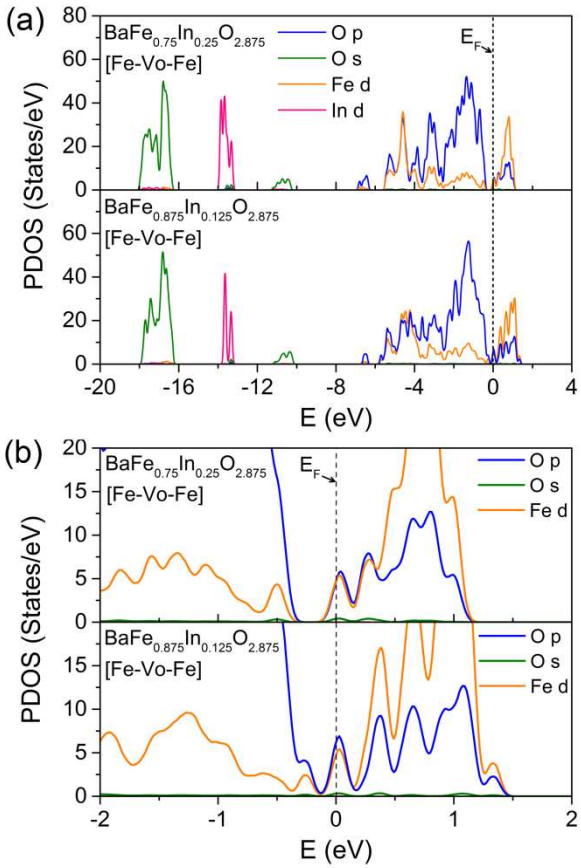

that there have two possible locations in both models. Parts of the oxygen ions and vacancies between two adjacent Fe atoms are denoted as [Fe-O-Fe] and [Fe-Vo-Fe], while the others between Fe and In are denoted as [In-O-Fe] and [In-Vo-Fe], respectively. Thus, there will be four possible transport paths for either models and the calculated values of the energies are listed in Table 5. Among them, the transport paths from [Fe-O-

Fig. 12 (a) (PDOS) on Fe(d), O(p), O(s) and In(d) orbitals; (b) Zoom-in near the Femi level.

Fe] to [Fe-Vo-Fe] have the minimum migration barrier of 1.29 eV and 2.07 eV, respectively, and these values, are much lower than the other paths, in which indium atoms are involved. From a point of view of energy, the oxygen vacancies are most likely to travel through the paths avoiding indium atoms. And as expected, with doubling of the indium content, the migration barrier energies for $BaFe_{0.75}In_{0.25}O_3$ are generally larger than these for $BaFe_{0.875}In_{0.125}O_3$, even for the most favourable [Fe-O-Fe]-[Fe-Vo-Fe] path. The obtained results imply that indium atoms would cause a decrease of the mobility of the oxygen anions, which is consistent with the effect of lattice free volume and membrane measurements, as shown in section 3.6.

Fig. 12 displays the projected densities of states (PDOS) for $BaFe_{0.875}In_{0.125}O_{2.875}$ and $BaFe_{0.75}In_{0.25}O_{2.875}$ super cells with an oxygen vacancy on the [Fe-Vo-Fe] site which is likely the most favourable defect in the energetic point of view. Total PDOS on Fe(d), O(p), O(s) and In(d) orbitals are shown in Fig. 12a and zoom-in near the Femi level are depicted in Fig. 12b.The 2p state of O strongly overlaps with the 3d state of Fe and both of them cross the Femi level as shown by dashed lines. The hybridized states above the Femi level provide extra electron density along the Fe-O-Fe bonds to form the transmission channel which is consistent with the high electronic conductivity of $BaFe_{1-x}In_xO_{3-\delta}$ materials as shown in Fig. 6. But, as can be seen from the Fig. 12b, the increment of dopant (In) slightly decayed the availability of empty states just above the Fermi level at the edge of the conduction bands, since the 3d state of In not hybridize with the 2p state of O and also less contributions the 3d states of Fe make. Such changes of band structure will jeopardize the electronic conductivity of $BaFe_{1-x}In_xO_{3-\delta}$ materials and the feature is agreed well with the decreased conductivity with increasing In content.

3.8 Structural stability

In the actual applications, one side of the membrane is often exposed to the reducing atmosphere. In consequence, good structural stability in a wide oxygen partial pressure range is essential to ensure high oxygen permeability in real operating

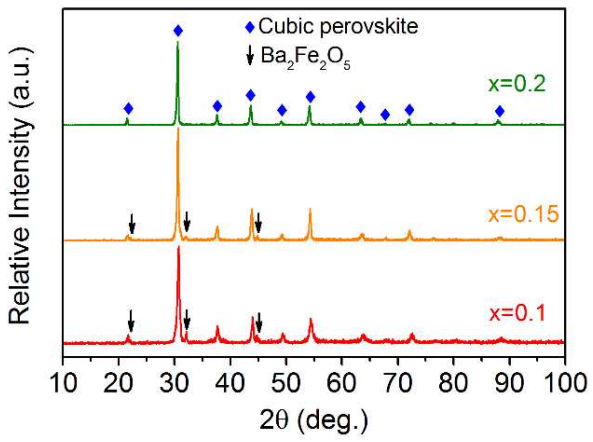

Fig. 13 XRD results recorded for surface of dense $BaFe1-xIn_xO_{3-\delta}$ samples after heat treatment in 5% H2/Ar at 900 °C for 10 h.

conditions. In order to evaluate reduction resistance of the considered $BaFe_{1-x}In_xO_{3-\delta}$ materials, samples with x = 0.1-0.2 were heat-treated in a furnace in 5 vol.% H_2/Ar atmosphere at 900 °C for 10 h, and the XRD patterns of their surface were measured, as presented in Fig. 13. While the main, perovskite-type structure was maintained after the heat treatment, presence of some small impurity peaks could be observed for $BaFe_{0.9}In_{0.1}O_{3-\delta}$ and $BaFe_{0.85}In_{0.15}O_{3-\delta}$ oxides. These peaks could be assigned to $Ba_2Fe_2O_5$ phase with a monoclinic structure. With an increasing indium content the impurity peaks disappear, implying that In can strengthen stability of $BaFe_{1-x}In_xO_{3-\delta}$ materials in reducing atmospheres. Taking the continuous re-oxidation by the transferred oxygen ions into consideration, the exact value of the oxygen partial pressure on the permeated side is in fact much higher than that in 5% H_2/Ar atmosphere.[30] Therefore, the extent of decomposition, which shown in Fig. 13, is exaggerated, and the $BaFe_{1-x}In_xO_{3-\delta}$ materials can be regarded as good candidates for the oxygen permeation membranes with a wide application prospects. It can be also stated that the reported series of materials exhibit possesses excellent structural stability, in contrast to most of the Co-based materials.

4 Conclusions

$BaFe_{1-x}In_xO_{3-\delta}$ ($0.05 \leq x \leq 0.2$) oxides were synthesized by the conventional solid-state reaction. Indium, partially substituting Fe at the B-site of $BaFe_{1-x}In_xO_{3-\delta}$, owing to its larger ionic radius, effectively decreases the tolerance factors of the materials, and in consequence, perovskite-type crystal structure is stabilized, of which samples with $x \geq 0.1$ are cubic in whole studied temperature range. The cubic $BaFe_{1-x}In_xO_{3-\delta}$ oxides exhibit good structural stability, with no phase changes, even at high temperatures, as verified by HT-XRD studies. With the increasing In content, oxygen release process was significantly suppressed and a decrease of thermal expansion coefficients was observed, however, due to disruption of the charge transfer channels, a decrease of the electrical conductivity was also recorded. $BaFe_{0.9}In_{0.1}O_{3-\delta}$ with cubic perovskite structure exhibits the best oxygen permeability among materials in the series, and structural analysis, as well as first principles calculations reveal that further doping with In leads to a decrease of the oxygen vacancy concentration and the oxygen ions mobility. The highest oxygen permeation flux of 1.11 mL cm^{-2} min^{-1} for 1.0 mm thin $BaFe_{0.9}In_{0.1}O_{3-\delta}$ membrane was measured at 950 °C under an air/He gradient. Studies of the influence of thickness of the membrane on the oxygen permeation flux indicate that the bulk diffusion is the rate-limiting step when membranes were thicker than 0.8 mm, however, for thinner membranes, the surface oxygen exchange become important, and eventually dominant. Results of XRD measurement of surface of $BaFe_{1-x}In_xO_{3-\delta}$ after heat treatment in reducing atmosphere suggest that indium is beneficial for the structural stability.

Finally, $BaFe_{0.9}In_{0.1}O_{3-\delta}$ composition can be selected as the most promising one for manufacturing of membranes for oxygen separation and partial oxidation of methane, especially due to its impressive oxygen permeability and good structural stability.

Acknowledgements

This work was financially supported by National Basic Research Program of China (2013CB934003), Guangdong Industry-Academy-Research Alliance (2012B091100129), National Nature Science Foundation of China (51452002), the Program of Introducing Talents of Discipline to Universities (B14003) and the Fundamental Research Funds for the Central Universities (FRF-IC-14-001).

Notes and references

[a] School of Materials Science and Engineering, University of Science and Technology Beijing, 30 Xueyuan Road, Beijing 100083, China, E-mail: hlzhao@ustb.edu.cn; Fax: +86 10 82376837; Tel: +86 10 82376837
[b] Department of Hydrogen Energy, Faculty of Energy and Fuels, AGH University of Science and Technology, al. A . Mickiewicza 30, 30-059 Krakow, Poland
[c] Beijing Key Lab of New Energy Materials and Technologies, 30 Xueyuan Road, Beijing 100083, China

1 J. Sunarso, S. Baumann, J. M. Serra, W. A. Meulenberg, S. Liu, Y. S. Lin and J. C. Diniz da Costa, *J. Membr. Sci.*, 2008, **320**, 13.
2 K. Zhang, J. Sunarso, Z. Shao, W. Zhou, C. Sun, S. Wang and S. Liu, *RSC Adv.*, 2011, **1**, 1661.
3 X. Zhu, H. Wang and W. Yang, *Solid State Ionics*, 2006, **177**, 2917.
4 A. J. Jacobson, *Chem. Mater.*, 2010, **22**, 660.
5 Z. Shao and S. M. Haile, *Nature*, 2004, **431**, 170.
6 Z. Du, H. Zhao, Y. Shen, L. Wang, M. Fang, K. Świerczek and K. Zheng, *J. Mater. Chem. A*, 2014, **2**, 10290.
7 H. J. M. Bouwmeester, *Catal. Today*, 2003, **82**, 141.
8 Y. Wei, W. Yang, J. Caro and H. Wang, *Chem. Eng. J.*, 2013, **220**, 185.
9 A. S. Yu, J. M. Vohs and R. J. Gorte, *Energy Environ. Sci.*, 2014, **7**, 944.
10 P. M. Geffroy, J. Fouletier, N. Richet and T. Chartier, *Chem. Eng. Sci.,* 2013, **87**, 408.
11 M. Yashima, N. Sirikanda and T. Ishihara, *J. Am. Chem. Soc.*, 2010, **132**, 2385.
12 H. Luo, K. Efimov, H. Jiang, A. Feldhoff, H. Wang and J. Caro, *Angew. Chem., Int. Ed.*, 2011, **50**, 759.
13 V. V. Kharton, I. P. Marozau, N. P. Vyshatko, A. L. Shaula, A. P. Viskup, E. N. Naumovich and F. M. B. Marques, *Mater. Res. Bull.*, 2003, **38**, 773.
14 Y. Teraoka, H. M. Zhang, S. Furukawa and N. Yamazoe, *Chem. Lett.*, 1985, **11**, 1743.
15 Y. Teraoka, T. Nobunaga and N. Yamazoe, *Chem. Lett.*, 1988, **17**, 503.
16 Y. Teraoka, H. M. Zhang, K. Okamoto and N. Yamazoe, *Mater. Res. Bull.*, 1988, **23**, 51.
17 L. Qiu, T. H. Lee, L. M. Liu, Y. L. Yang and A. J. Jacobson, *Solid State Ionics*, 1995, **76**, 321.
18 L. M. Liu, T. H. Lee, L. Qiu, Y. L. Yang and A. J. Jacobson, *Mater. Res. Bull.*, 1996, **31**, 29.
19 Z. Shao, G. Xiong, J. Tong, H. Dong and W. Yang, *Sep. Purif. Technol.*, 2001, **25**, 419.
20 K. Efimov, Q. Xu and A. Feldhoff, *Chem. Mater.*, 2010, **22**, 5866.
21 F. Liang, H. Jiang, H. Luo, J. Caro and A. Feldhoff, *Chem. Mater.*, 2011, **23**, 4765.
22 P. Müller, H. Störmer, M. Meffert, L. Dieterle, C. Niedrig, S. F. Wagner, E. Ivers-Tiffée and D. Gerthsen, *Chem. Mater.*, 2013, **25**, 564.
23 S. McIntosh, J. F. Vente, W. G. Haije, D. H. A. Blank and H. J. M. Bouwmeester, *Chem. Mater.*, 2006, **18**, 2187.
24 L. Yang, Z. Wu, W. Jin and N. Xu, *Ind. Eng. Chem. Res.*, 2004, **43**, 2747.
25 Y. Cheng, H. Zhao, D. Teng, F. Li, X. Lu and W. Ding, *J. Membr. Sci.*, 2008, **322**, 484.
26 H. Luo, B. Tian, Y. Wei, H. Wang, H. Jiang and J. Caro, *AIChE J.*, 2010, **56**, 604-610.
27 H. Wang, C. Tablet, A. Feldhoff and J. Caro, *Adv. Mater.*, 2005, **17**, 1785.
28 K. Efimov, T. Halfer, A. Kuhn, P. Heitjans, J. Caro and A. Feldhoff, *Chem. Mater.*, 2010, **22**, 1540.
29 J. Martynczuk, F. Liang, M. Arnold, V. Šepelák and A. Feldhoff, *Chem. Mater.*, 2009, **21**, 1586.
30 X. Zhu, Y. Cong and W. Yang, *J. Membr. Sci.*, 2006, **283**, 38.
31 T. Kida, D. Takauchi, K. Watanabe, M. Yuasa, K. Shimanoe, Y. Teraoka and N. Yamazoe, *J. Electrochem. Soc.*, 2009, **156**, E187.
32 T. Kida, A. Yamasaki, K. Watanabe, N. Yamazoe and K. Shimanoe, *J. Solid State Chem.*, 2010, **183**, 2426.
33 X. Liu, H. Zhao, J. Yang, Y. Li, T. Chen, X. Lu, W. Ding and F. Li, *J. Membr. Sci.*, 2011, **383**, 235.
34 F. Liang, K. Partovi, H. Jiang, H. Luo and J. Caro, *J. Mater. Chem. A*, 2013, **1**, 746.
35 D. Xu, F. Dong, Y. Chen, B. Zhao, S. Liu, M. O. Tade and Z. Shao, *J. Membr. Sci.*, 2014, **455**, 75.
36 P. M. Geffroy, A. Vivet, L. Nguyen, E. Blond, N. Richet and T. Chartier, *J. Eur. Ceram. Soc.*, 2013, **33**, 1849.
37 F. Dong, D. Chen, Y. Chen, Q. Zhao and Z. Shao, *J. Mater. Chem.*, 2012, **22**, 15071.
38 F. Dong, Y. Chen, R. Ran, D. Chen, M. O. Tade, S. Liu and Z. Shao, *J. Mater. Chem. A*, 2013, **1**, 9781.
39 R. D. Shannon, *Acta Crystallogr. Sect. A*, 1976, **32**, 751.
40 V. M. Goldschmidt, *Naturwissenschaften*, 1926, **14**, 477.
41 Y. Li, H. Zhao, N. Xu, Y. Shen, X. Lu, W. Ding and F. Li, *J. Membr. Sci.*, 2010, **362**, 460.
42 A. C. Larsen and R. B. Von Dreele, *General Structure Analysis System*, Los Alamos National Laboratory Report LAUR 86-748, New Mexico, USA, 2004.
43 B. H. Toby, *J. Appl. Cryst.*, 2001, **34**, 210.
44 M. D. Segall, J. D. L. Philip, M. J. Probert, C. J. Pickard, P. J. Hasnip, S. J. Clark and M. C. Payne, *J. Phys.: Condens. Matter*, 2002, **14**, 2717.
45 S. J. Clark, M. D. Segall, C. J. Pickard, P. J. Hasnip, M. I. Probert, K. Refson and M. C. Payne, *Zeitschrift für Kristallographie*, 2005, **220**, 567.

46 J. P. Perdew, K. Burke and M. Ernzerhof, *Phys. Rev. Lett.*, 1996, **77**, 3865.
47 B. G. Pfrommer, M. Côté, S. G. Louie and M. L. Cohen, *J. Comput. Phys.*, 1997, **131**, 233.
48 X. Zhang, C. Fan, Y. Wang, Y. Wang, Z. Liang and P. Han, *Comput. Mater. Sci.*, 2013, **71**, 135.
49 A. Feldhoff, J. Martynczuk, M. Arnold, M. Myndyk, I. Bergmann, V. Šepelák, W. Gruner, U. Vogt, A. Hähnel and J. Woltersdorf, *J. Solid State Chem.*, 2009, **182**, 2961.
50 F. Dong, Y. Chen, D. Chen and Z. Shao, *ACS Appl. Mater. Interfaces*, 2014, **6**, 11180.
51 X. Chen, J. Yu and S. B. Adler, *Chem. Mater.*, 2005, **17**, 4537.
52 X. Chen and T. Grande, *Chem. Mater.*, 2013, **25**, 927.
53 Z. Shao, W. Yang, Y. Cong, H. Dong, J. Tong and G. Xiong, *J. Membr. Sci.*, 2000, **172**, 177.
54 J. Tong, W. Yang, B. Zhu and R. Cai, *J. Membr. Sci.*, 2002, **203**, 175.
55 Z. Wu, X. Dong, W. Jin, Y. Fan and N. Xu, *J. Membr. Sci.*, 2007, **291**, 172.
56 H. L. Lein, K. Wiik and T. Grande, *Solid State Ionics*, 2006, **177**, 1795.
57 S. Li, Z. Lü, X. Huang, B. Wei and W. Su, *J. Phys. Chem. Solids*, 2007, **68**, 1707.
58 A. A. Yaremchenko, E. V. Tsipis, A. V. Kovalevsky, J. C. Waerenborgh and V. V. Kharton, *Solid State Ionics*, 2011, **192**, 259.
59 B. Wei, Z. Lü, S. Li, Y. Liu, K. Liu and W. Su, *Electrochem. Solid-State Lett.*, 2005, **8**, A428.
60 B. Wei, Z. Lü, X. Huang, M. Liu, N. Li and W. Su, *J. Power Sources*, 2008, **176**, 1.
61 H. Zhao, N. Xu, Y. Cheng, W. Wei, N. Chen, W. Ding, X. Lu and F. Li, *The J. Phys. Chem. C*, 2010, **114**, 17975.
62 C. Zener, *Phys. Rev.*, 1951, **81**, 440.
63 R. L. Cook and A. F. Sammells, *Solid State Ionics*, 1991, **45**, 311.
64 A. F. Sammells, R. L. Cook, J. H. White, J. J. Osborne and R. C. MacDuff, *Solid State Ionics*, 1992, **52**, 111.
65 C. Wagner and W. Schottky, *Z. Physik. Chem*, 1930, **11**, 163.
66 M. S. Islam, *J. Mater. Chem.*, 2000, **10**, 1027.
67 M. Cherry, M. S. Islam and C. R. A. Catlow, *J. Solid State Chem.*, 1995, **118**, 125.

An impressive oxygen permeability and good structural stability is achieved by partially replacing Fe with In at B-stie of $BaFeO_{3-\delta}$ oxides.